



Spitzer Opens New Path to Break Classic Degeneracy for Jupiter-mass Microlensing Planet OGLE-2017-BLG-1140Lb

S. Calchi Novati¹ , J. Skowron² , Y. K. Jung³,

and

C. Beichman⁴, G. Bryden⁵, S. Carey⁶, B. S. Gaudi⁷ , C. B. Henderson⁸, Y. Shvartzvald^{5,17}, J. C. Yee⁹, W. Zhu¹⁰

(Spitzer Team),

A. Udalski², M. K. Szymański², P. Mróz², R. Poleski^{2,7} , I. Soszyński², S. Kozłowski² , P. Pietrukowicz² , K. Ulaczyk²,M. Pawlak², K. Rybicki², P. Iwanek²

(OGLE Collaboration),

and

M. D. Albrow¹¹, S.-J. Chung^{3,12} , A. Gould^{3,7,13}, C. Han¹⁴, K.-H. Hwang³ , Y.-H. Ryu³ , I.-G. Shin⁹ , W. Zang¹⁵, S.-M. Cha^{3,16}, D.-J. Kim³, H.-W. Kim³, S.-L. Kim^{3,12}, C.-U. Lee^{3,12}, D.-J. Lee³, Y. Lee^{3,16}, B.-G. Park^{3,12}, and R. W. Pogge⁷

(KMTNet Collaboration)

¹ IPAC, Mail Code 100-22, Caltech, 1200 E. California Blvd., Pasadena, CA 91125, USA² Warsaw University Observatory, Al. Ujazdowskie 4, 00-478 Warszawa, Poland³ Korea Astronomy and Space Science Institute, Daejeon 34055, Republic of Korea⁴ NASA Exoplanet Science Institute, California Institute of Technology, Pasadena, CA 91125, USA⁵ Jet Propulsion Laboratory, California Institute of Technology, 4800 Oak Grove Drive, Pasadena, CA 91109, USA⁶ Spitzer, Science Center, MS 220-6, California Institute of Technology, Pasadena, CA, USA⁷ Department of Astronomy, Ohio State University, 140 W. 18th Ave., Columbus, OH 43210, USA⁸ IPAC/NEExSci, Mail Code 100-22, Caltech, 1200 E. California Blvd., Pasadena, CA 91125, USA⁹ Harvard-Smithsonian Center for Astrophysics, 60 Garden St., Cambridge, MA 02138, USA¹⁰ Canadian Institute for Theoretical Astrophysics, University of Toronto, 60 St George Street, Toronto, ON M5S 3H8, Canada¹¹ University of Canterbury, Department of Physics and Astronomy, Private Bag 4800, Christchurch 8020, New Zealand¹² Korea University of Science and Technology, Daejeon 34113, Republic of Korea¹³ Max-Planck-Institute for Astronomy, Königstuhl 17, D-69117 Heidelberg, Germany¹⁴ Department of Physics, Chungbuk National University, Cheongju 28644, Republic of Korea¹⁵ Physics Department and Tsinghua Centre for Astrophysics, Tsinghua University, Beijing 100084, People's Republic of China¹⁶ School of Space Research, Kyung Hee University, Yongin, Kyeonggi 17104, Republic of Korea

Received 2018 March 12; revised 2018 April 20; accepted 2018 April 30; published 2018 June 1

Abstract

We analyze the combined *Spitzer* and ground-based data for OGLE-2017-BLG-1140 and show that the event was generated by a Jupiter-class ($m_p \simeq 1.6 M_{\text{Jup}}$) planet orbiting a mid-late M dwarf ($M \simeq 0.2 M_{\odot}$) that lies $D_{\text{LS}} \simeq 1.0$ kpc in the foreground of the microlensed Galactic-bar source star. The planet–host projected separation is $a_{\perp} \simeq 1.0$ au, i.e., well beyond the snow line. By measuring the source proper motion μ_s from ongoing long-term OGLE imaging and combining this with the lens-source relative proper motion μ_{rel} derived from the microlensing solution, we show that the lens proper motion $\mu_l = \mu_{\text{rel}} + \mu_s$ is consistent with the lens lying in the Galactic disk, although a bulge lens is not ruled out. We show that while the *Spitzer* and ground-based data are comparably well fitted by planetary (i.e., binary-lens (2L1S)) and binary-source (1L2S) models, the combination of *Spitzer* and ground-based data decisively favors the planetary model. This is a new channel to resolve the 2L1S/1L2S degeneracy, which can be difficult to break in some cases.

Key words: gravitational lensing: micro

1. Introduction

The degeneracy between binary-lens/single-source (2L1S) and single-lens/binary-source (1L2S) microlensing events, first noted by Gaudi (1998), has continually grown in importance and complexity over the first 15 yr of microlensing-planet detections, particularly as these have reached toward lower planet–host mass-ratio planets. As originally formulated by Gaudi (1998), a 1L2S event can mimic a 2L1S event if the second source is much fainter than the first and the lens happens to pass much closer to it. In this case, the second source gives rise to a smooth, short-lived, low-amplitude bump as it very briefly becomes highly magnified. Any putative

planetary signal that is consistent with such a smooth short-lived bump must therefore be vetted against the 1L2S explanation. This already became an issue for the third microlensing planet, OGLE-2005-BLG-390Lb (Beaulieu et al. 2006), for which the smooth bump was actually generated by a “Cannae”-type “Hollywood” event (Hwang et al. 2018), in which a very large source completely envelops the planetary caustic. For the actual case of OGLE-2005-BLG-390Lb, the 1L2S solution was ruled out ($\Delta\chi^2 > 50$). However, in the course of their systematic study of all archival low-mass-ratio ($q < 10^{-4}$) microlensing planets, Udalski et al. (2018) showed that, had the mass ratio been smaller, $\log(q'/q) < -0.2$, the 2L1S and 1L2S models could not have been reliably distinguished.

¹⁷ NASA Postdoctoral Program Fellow.

Over the years, it has become clear that a variety of other microlensing-planet geometries can induce smooth bumps that can potentially be confused with 1L2S geometries. Bond et al. (2017) and Shvartzvald et al. (2017) analyzed a smooth bump in OGLE-2016-BLG-1195 and showed that it was due to the source passing over a smooth “ridge” in the magnification pattern between the central and planetary caustic (“wide-planet” solution) or over a smooth ridge extending from the central caustic (“close-planet” solution). Again, however, Udalski et al. (2018) showed that the 2L1S and 1L2S solutions could not have been distinguished if the planet mass ratio had been lower by $\log(q'/q) < -0.3$.

Both of these forms of the degeneracy are likely to become more important in the future. Zhu et al. (2014) showed that in the era of pure-survey microlensing-planet detections, half of all “detectable” planets (based on the χ^2 criterion) are likely to be non-caustic crossing events (i.e., broadly similar to OGLE-2016-BLG-1195), which will generically induce smooth bumps, as opposed to the sudden jumps that usually characterize caustic crossings, which are present in a substantial majority of published planetary microlensing events. Moreover, it is not necessary to fully envelop the caustic to produce a smooth bump in a caustic-crossing event: Hwang et al. (2018) showed that “von Schlieffen”-type Hollywood events, in which the source only partially envelops the caustic, can produce very similar light curves to “Cannae” events.¹⁸

Furthermore, new forms of this degeneracy are being discovered. Jung et al. (2017) showed that a 1L2S event with a source-flux ratio $q_f \simeq 2$ could be broadly mimicked by a planetary microlensing geometry. In this case, the 2L1S geometry was ruled out by $\Delta\chi^2 > 500$, so strictly speaking, the solutions were not “degenerate.” Nevertheless, the fact that much more complex binary-lens structures than “short-lived bumps” can be mimicked by binary-source geometries should serve as a broad caution when analyzing events.

Finally, Hwang et al. (2017) found yet another path to this degeneracy in their analysis of OGLE-2015-BLG-1459. The first point to note about this event is that it had a threefold degeneracy: 3L1S versus 2L2S versus 1L3S. In the triple-lens model, the third body was a “moon” that was detected in only one magnified point (albeit a 0.4 mag deviation detected with very high confidence). Such single-point (or even few-point) deviations due to a planet can easily be confused with a “smooth bump,” even if the underlying light curve would reveal a pronounced caustic structure, just because of poor sampling.

The first line of defense against the 2L1S/1L2S degeneracy is simply $\Delta\chi^2$ between the two models. A few cases were mentioned above, but there are many others as well (e.g., Han et al. 2018). However, as discussed above, in the few published cases of low- q events that were investigated by Udalski et al. (2018), the threshold for resolving this degeneracy did not lie far below the actual value of q .

¹⁸ As discussed at somewhat greater length by Skowron et al. (2018), the term “Hollywood” was coined by Gould (1997) to emphasize the virtues of “following the big stars” because they have a large cross section for completely enveloping the planetary caustic. Later, Hwang et al. (2018) distinguished between full (“Cannae”) and partial (“von Schlieffen”) envelopment, in analogy to the military strategies of Hannibal at Cannae and the “von Schlieffen plan” in World War I.

A second line of defense is to measure the color difference of the (putative) two sources. Because light travels on geodesics, microlensing is intrinsically achromatic. The only exception¹⁹ would be if two stars (or two parts of a single star) were of different colors and magnified by different amounts. The latter effect can occur if a single star is transited by a point lens or a caustic from a binary lens. However, this is rather weak. Substantial chromaticity requires two sources of substantially different color and magnified by different amounts. The short-term “smooth bumps” that are the main source of ambiguity are well suited to this test. Recall that the 1L2S model generally requires that one of the sources is much fainter than the other and also much more highly magnified. Generally, fainter sources are redder (particularly if the brighter source is on the main sequence (MS)), so the light during the bump should be redder than on the rest of the light curve. For example, Hwang et al. (2017) confirmed the 1L3S interpretation using this effect for OGLE-2015-BLG-1459. However, if the primary source is a giant, then the secondary can have a similar color even if it is several orders of magnitude fainter. Moreover, as mentioned above, there are cases for which the source-flux ratio is actually close to unity (Jung et al. 2017). But the main impediment to this method is simply that alternate- (usually V -) band data are not typically taken at a high enough cadence to accurately measure the color of a short-lived smooth bump.

Here we use *Spitzer* observations of the planetary microlensing event OGLE-2017-BLG-1140 to demonstrate the power of a new method to resolve the 2L1S/1L2S degeneracy that is based on space-based microlensing parallax.

2. Observations

OGLE-2017-BLG-1140 is at (R.A., decl.) = (17:47:31.93, $-24:31:21.6$), corresponding to $(l, b) = (4.0, 1.9)$. It was discovered and announced as a probable microlensing event by the OGLE Early Warning System (Udalski et al. 1994; Udalski 2003) at UT 11:57 on 2017 June 19. The event lies in OGLE field BLG633 (Udalski et al. 2015a), for which OGLE observations were at a characteristic cadence of $\Gamma = 1 \text{ day}^{-1}$ using their 1.3 m telescope at Las Campanas, Chile.

The Korea Microlensing Telescope Network (KMTNet; Kim et al. 2016) observed this field from its three 1.6 m telescopes at CTIO (Chile, KMTC), SAAO (South Africa, KMTS), and SSO (Australia, KMTA) in its BLG19 field, implying that it was observed at a cadence of $\Gamma = 1 \text{ hr}^{-1}$ during the *Spitzer* season. The event was identified by KMTNet as SSO19M0601.004271.

The great majority of ground-based observations were carried out in the I band with occasional V -band observations made solely to determine source colors. All reductions for the light-curve analysis were conducted using variants of difference image analysis (DIA; Tomaney & Crofts 1996; Alard & Lupton 1998), specifically Woźniak (2000) and Albrow et al. (2009).

The event was also observed by *Spitzer*. As discussed in detail by Yee et al. (2015), *Spitzer* selections can be “objective,” “subjective,” or “secret,” which impacts how detected planets (and planet sensitivity) enter the *Spitzer* program to measure the Galactic distribution of planets (Gould et al. 2013, 2014, 2015a, 2015b, 2016). Events that meet

¹⁹ In fact, interference effects in microlensing (so-called “femtolensing”; Gould 1992a) can also generate chromatic effects. However, this is not a practical issue for Galactic microlensing studies.

certain prespecified objective criteria must be observed, and consequently all planets detected during the event can enter the program sample. Events can be selected “subjectively” by the team for any reason and at any time. However, only planets (and simulated planets needed to calculate planet sensitivity) that do not generate significant signal in the data available at the time of the public announcement can enter the sample. The observational cadence and the conditions for stopping the observations must be specified at the time of the announcement. Events can also be chosen “secretly,” i.e., without announcement, and then later changed to “subjective” (if such a decision is subsequently made). In this case, the constraints on what is a “detectable” planet apply according to the date of the “subjective” announcement. Moreover, *Spitzer* observations taken before this date cannot be included in the determination of whether the microlens parallax is measured well enough to enter the sample (Zhu et al. 2017).

OGLE-2017-BLG-1140 was chosen “secretly,” at UT 13:08 on June 19, i.e., slightly more than 1 hr after it was announced by OGLE and about 8 minutes before the first *Spitzer* “upload” (i.e., when target coordinates are sent to *Spitzer* operations²⁰). This selection was made by the upload subteam because the event appeared to be consistent with reaching relatively high magnification based on the data available at that time. The upload subteam does not generally have the authority to choose events subjectively without giving the whole team an opportunity for a joint decision. The target entered the *Spitzer* Sun-angle window roughly 1.65 days after the first *Spitzer* observation, i.e., at UT 07:08 on June 24. The event was announced “subjectively” at UT 16:23 on June 25, i.e., about 33 hr later.²¹ Therefore, all *Spitzer* observations in this interval must be excluded from the determination of whether the *Spitzer* parallax is well measured, and of course if a planetary anomaly proves significantly detectable ($\Delta\chi^2 = 10$) from data available prior to this announcement ($\text{HJD}' \equiv \text{HJD} - 2,450,000 = 7930.19$), then the planet must be excluded from the Galactic distribution sample.

In fact, these restrictions have almost no practical effect. There were only four *Spitzer* observations taken in this interval,

²⁰ <http://ssc.spitzer.caltech.edu>

²¹ This decision was made because it was realized (based on “quick-look” KMTNet data) that the event would become “objective” 21 hr later at the next *Spitzer* upload. Note that events can only become “objective” at the times of uploads. Note also that, according to the Yee et al. (2015) protocols as they operated at the time of this decision, if the event had simply been “allowed” to become “objective” (i.e., without “subjective” announcement), then the *Spitzer* data taken prior to the first spacecraft commands (UT 23:52, June 29) that were uploaded on that date (June 26) could not enter the Zhu et al. (2017) test to determine whether the parallax had been measured well enough to enter the sample. In fact, this is a shortcoming of these protocols, which we now modify for future events as follows: if an event goes from “secret” to “objective” (and unless otherwise publicly specified by the team), then it automatically becomes “subjective” at the upload time as well, with the cadence and conditions being identical to those of “objective” events. In this case, the usual Yee et al. (2015) algorithm for resolving conflicts between “subjective” and “objective” designations is applied. In particular, if the *Spitzer* data from after the upload triggered by the “objective” designation are adequate for measuring the parallax according to the Zhu et al. (2017) criteria, then all planets discovered in the event can enter the sample. However, if meeting these criteria requires earlier *Spitzer* data (but still taken after the event became “objective”), then only planets that do not generate significant signals in data available before this date can be included. It may appear to be simple enough to make the appropriate announcement on or before the date that the event becomes “objective” (as was done in the present case). However, in practice, “secret” events receive less scrutiny during the hectic process of evaluating hundreds of events in preparation for upload because they do not require observing decisions. See Ryu et al. (2018) for a relevant example.

and they do not contribute significantly to the parallax measurement. The last ground-based data point available at the time of the announcement was at $\text{HJD}' = 7928.61$, at which point the light curve was perfectly consistent with a point lens. The event was first suspected to be anomalous on July 5, but in retrospect, this appears to be based on some points near peak that were impacted by close passage of the Moon. The anomaly was first recognized as due to a weak 2L1S perturbation or a 1L2S geometry on July 13 based on ground-based data. However, at that point, and also at a subsequent update when the event reached baseline, the 2L1S/1L2S degeneracy appeared insurmountable. The decision to pursue the analysis was made after inspecting the anomaly in the *Spitzer* data.

The *Spitzer* data were reduced using specially designed software (Calchi Novati et al. 2015b).

We follow the standard procedure (e.g., Yee et al. 2012) of rescaling error bars so that the χ^2/dof for each data set is of order unity for the best model. For OGLE and KMTNet, the rescaling factors are in the range 1.3–1.5; for *Spitzer*, we evaluate a factor 2.6.

3. Light-curve Analysis

At a glance, OGLE-2017-BLG-1140 deviates from the smooth, symmetric (single) point-source–point-lens (1L1S) Paczyński (1986) shape. This is obvious from inspection of the *Spitzer* light curve, somewhat less so for ground-based data (see Figure 1). Still, for ground-based data only, a 1L1S model has a $\Delta\chi^2 = 915$ from the best planetary model discussed below, and the systematic deviations from the data are clearly visible in the bottom panel of Figure 1. Based on the general appearance of its light curve, OGLE-2017-BLG-1140 could, in principle, be either 2L1S or 1L2S. However, because the correct model is actually 2L1S, we focus on that here and defer discussion of 1L2S models to Section 5.

We will eventually show that 2L1S solutions could be derived from either the ground-based or *Spitzer* data. However, we begin by reporting our actual path toward deriving the solution. As in the case of OGLE-2017-BLG-1130 (Wang et al. 2018), the binarity of the lens is much more apparent by eye in the *Spitzer* data, so we begin by conducting a grid search using these data only. The lens system is reasonably well described by six parameters ($t_0, u_0, t_E, s, q, \alpha$). The first three (Paczynski 1986) parameters are, respectively, the time of closest approach to the center of mass, the impact parameter (normalized to θ_E), and the Einstein timescale, i.e., $t_E = \theta_E/\mu_{\text{rel}}$, where μ_{rel} is the lens-source relative proper motion. The final three are the planet–host separation (in units of θ_E), the planet–host mass ratio, and the angle between the instantaneous planet–host axis and μ . In fact, as we will show shortly, a seventh parameter can also be measured: $\rho \equiv \theta_*/\theta_E$, where θ_* is the angular radius of the source. However, in order to quantify the robustness of this measurement and facilitate understanding of the information flow, we initially set $\rho = 0$. In addition to these six geometric parameters, there are two flux parameters ($f_{s,j}, f_{b,j}$) for each observatory, j . That is, we model the flux observed at each time t_i by the j th observatory as $F_j(t_i) = f_{s,j}A(t_i; t_0, u_0, t_E, s, q, \alpha) + f_{b,j}$.

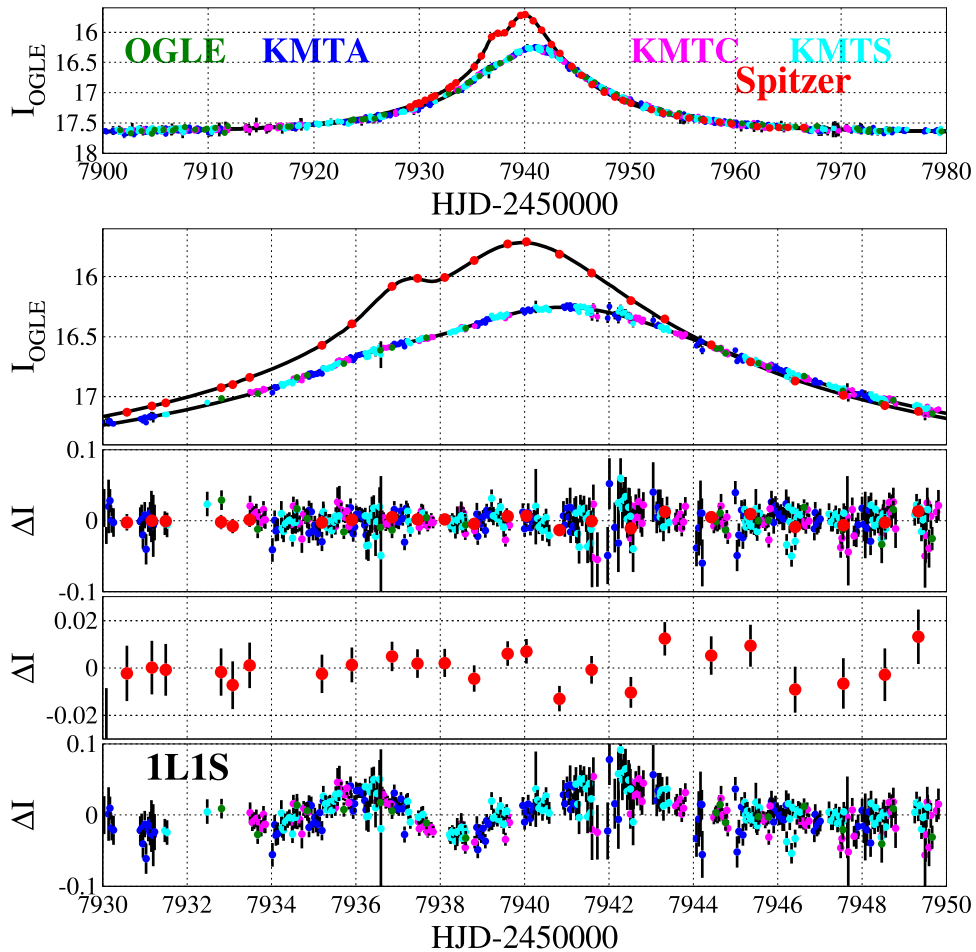


Figure 1. Light curve and 2L1S model and residuals of OGLE-2017-BLG-1140 (first four panels). The overall difference between the *Spitzer* (which is transformed for display to the *I*-band magnitude system) and ground-based (OGLE, KMTA, KMTC, and KMTS) data yields the microlens parallax vector π_E . More subtle differences, such as the strength of the pre-peak “smooth bump” anomaly in both data sets, allow one to decisively rule out the competing class of 1L2S models. Note that the *Spitzer* residuals are shown again, separately, in the bottom panel because their error bars are substantially smaller than the range that must be displayed on the main residual panel. Bottom panel: residuals for 1L1S model for ground-based data only.

3.1. Six-parameter Solutions ($\rho = 0$)

The binary-lens model is specified by the parameters of the caustic, (s, q) , and the angle of the trajectory, α . In the caustic region, because of the divergences in the magnification map, the χ^2 topology is, however, extremely complex and may present sharp variations along these parameters. Therefore, standard minimization procedures including Markov chain Monte Carlo (MCMC) are not suitable tools to locate, starting from a generic position in the parameter space, the absolute minimum. This is not the case, on the other hand, for the single-lens parameters for which the χ^2 surface is smooth (in particular, this holds for ρ and explains why we run the grid with $\rho = 0$). This is the reason why, lacking a plausible a priori intuition of the “right” binary-lens model, we start the analysis with a blind-search grid in the binary-lens parameter space. Once the χ^2 minimum is identified within the grid search, we run a final analysis with all the parameters left free to vary to fully characterize the solution. Specifically, we conduct a dense 40^3 grid search on $[0 \leq s < 2] \times [-4 \leq \log q < 0] \times [0 \leq \alpha < 2\pi]$, and for each such triple, we fit for the remaining three parameters.²² We model the light curves using the algorithm of

Bozza (2010), which has a publicly available implementation.²³ This grid search yields four minima at $(s, \log q) = (0.7, -1.8)$, $(0.8, -2.2)$, $(1.5, -2.2)$, and $(1.6, -1.4)$. We then seed these solutions into an MCMC (Dong et al. 2009) for which all parameters are allowed to vary. The two “close” ($s < 1$) seeds both converge to the same solution, which is given in Table 1. The remaining two solutions, which are the corresponding “wide” ($s > 1$) variants of the close/wide ($s \leftrightarrow s^{-1}$) degeneracy (Griest & Safizadeh 1998; Dominik 1999), also converge. However, these prove not to be viable, as we discuss further below.

To combine *Spitzer* and ground-based data, we must introduce two additional parameters: the two components of the vector microlens parallax (Gould 1992b, 2000),

$$\pi_E \equiv \frac{\pi_{\text{rel}}}{\theta_E} \frac{\boldsymbol{\mu}_{\text{rel}}}{\mu_{\text{rel}}}, \quad (1)$$

where $\pi_{\text{rel}} \equiv \text{au}(D_L^{-1} - D_S^{-1})$ is the lens-source relative parallax. We evaluate π_E in equatorial coordinates, i.e., $\pi_E = (\pi_{E,N}, \pi_{E,E})$.

We make an initial estimate of π_E by simultaneously fitting the ground and space data (with the anomaly excised) to a 1L1S

²² For the nonlinear fitting, we make use of MINUIT (James & Roos 1975) within the CERNLIB package <https://cernlib.web.cern.ch/cernlib/>.

²³ <http://www.fisica.unisa.it/GravitationAstrophysics/VBBinaryLensing.htm>

Table 1
2L1S Solutions with $\rho = 0$

Parameter	<i>Spitzer</i>	Ground	<i>Spitzer</i> and Ground	
χ^2/dof	44.8/35	2964.6/2936	3024.9/2975 (+, +)	3025.9/2975 (-, -)
t_0 [HJD—2,457,940.]	$-0.201^{+0.011}_{-0.011}$	$0.7645^{+0.0063}_{-0.0066}$	$0.7604^{+0.0060}_{-0.0062}$	$0.7606^{+0.0061}_{-0.0062}$
u_0	$0.1343^{+0.0083}_{-0.0082}$	$0.2373^{+0.0044}_{-0.0055}$	$0.2364^{+0.0040}_{-0.0042}$	$-0.2365^{+0.0042}_{-0.0040}$
t_E [days]	$14.58^{+0.68}_{-0.63}$	$14.74^{+0.17}_{-0.13}$	$14.74^{+0.14}_{-0.13}$	$14.74^{+0.14}_{-0.13}$
ρ	0	0	0	0
$\pi_{E,N}$	$-0.0793^{+0.0016}_{-0.0016}$	$0.0799^{+0.0016}_{-0.0016}$
$\pi_{E,E}$	$0.0524^{+0.0007}_{-0.0007}$	$0.0520^{+0.0007}_{-0.0007}$
α [rad]	$2.561^{+0.013}_{-0.013}$	$2.545^{+0.012}_{-0.011}$	$2.5463^{+0.0085}_{-0.0083}$	$-2.5462^{+0.0082}_{-0.0083}$
s	$0.815^{+0.019}_{-0.021}$	$0.855^{+0.017}_{-0.019}$	$0.831^{+0.012}_{-0.012}$	$0.831^{+0.012}_{-0.012}$
q	$0.0099^{+0.0015}_{-0.0013}$	$0.0079^{+0.0012}_{-0.0010}$	$0.0090^{+0.0009}_{-0.0008}$	$0.0090^{+0.0009}_{-0.0008}$
$f_{s,\text{OGLE}}$...	1.131 ± 0.024	1.127 ± 0.020	1.127 ± 0.020
$f_{b,\text{OGLE}}$...	0.237 ± 0.024	0.241 ± 0.020	0.241 ± 0.020
$f_{s,\text{Spitzer}}$	17.4 ± 1.1	...	17.4 ± 0.3	17.4 ± 0.3
$f_{b,\text{Spitzer}}$	2.4 ± 0.9	...	2.4 ± 0.3	2.5 ± 0.3
$I - L$	2.971 ± 0.007	2.971 ± 0.007

model. We then seed the resulting π_E and the *Spitzer*-based fit for the other six parameters (t_0 , u_0 , t_E , s , q , α) into a simultaneous fit to the ground-based and *Spitzer* data. The resulting solution is again shown in Table 1. This is the so-called “(+, +)” solution; see Section 3.2. In order to facilitate comparison with the results in that section, we also show the corresponding “(–, –)” solution. Finally, we remove the *Spitzer* data and fit for six parameters only (t_0 , u_0 , t_E , s , q , α) using the ground-based data. This solution is also shown in Table 1.

Comparing the three solutions (*Spitzer*-only, ground-only, and joint (+, +)), we see that they are nearly identical. There are only two major differences.²⁴ First, the joint solution has parallax parameters, whereas the others do not. Second, the values of (t_0 , u_0) for the *Spitzer*-only solution differ significantly from the other two, which agree with each other. These two differences reflect the fact that π_E can only be determined by comparing the ground-based and *Spitzer* light curves. This means, first, that these parameters appear only in the joint solution, and second, that the basis of the π_E measurement is the different values of (t_0 , u_0) as seen from the two telescope locations²⁵ (Refsdal 1966; Gould 1994).

We also investigate the “wide” solutions discussed above but find that they are strongly excluded. First, we repeat the entire procedure above but for the ground-only data. We find seven seed solutions, of which three converge in the MCMC to the same solution shown in Table 1. Of the remaining four, two converge to solutions with $\Delta\chi^2 > 150$, which we consider ruled out, and the other two converge to a “wide” variant from the ($s \leftrightarrow s^{-1}$) degeneracy, namely,

$$(s, \log q, \alpha) = (1.64 \pm 0.02, -2.31 \pm 0.04, 2.487 \pm 0.006) \quad (\text{wide; ground}). \quad (2)$$

This solution already has $\Delta\chi^2 = 135$ relative to the ground-only solution in Table 1. However, the main thing to note is that the (s , $\log q$, α) parameters are different from those reported from the *Spitzer*-only “wide” solution discussed above, which, stated more precisely, are

$$(s, \log q, \alpha) = (1.57 \pm 0.02, -2.03 \pm 0.04, 2.575 \pm 0.010) \quad (\text{wide; Spitzer}). \quad (3)$$

This discrepancy is related to the fact that, at next order in q (i.e., away from the $q \rightarrow 0$ limit), the ($s \leftrightarrow s^{-1}$) degeneracy is actually trajectory-specific (An 2005). That is, it becomes a one-dimensional (1D) degeneracy on a cut through the 2D magnification plane. See Figure 4 from Albrow et al. (2002) and Figure 8 from Afonso et al. (2000). Hence, when both ground-based and *Spitzer* data sets are fit jointly to the “wide” solution, they prove incompatible, with $\Delta\chi^2 = 522$ (compared to 2L1S), i.e., 358 higher than the sum of the two $\Delta\chi^2$ from the separate fits.

3.2. Seven-parameter Solutions (Free ρ)

Next, we allow ρ to vary freely in the MCMC, seeded by the *Spitzer*-only, ground-only, and joint (+, +) solutions from Table 1.²⁶ The best-fit parameters are shown in Table 2, and the geometry of the joint solution is shown in Figure 2. The “bump” in the *Spitzer* light curve is caused by the source passing over the ridge extending from a cusp of the central caustic. The ground-based light curve is also affected by this cusp passage, but because the source lies further from the cusp as seen from Earth, its effect on the light curve is not as easily discernible by eye. Nevertheless, as demonstrated by the similarity of the solutions in Tables 1 and 2, the ground-based

²⁴ The much more subtle differences in (s, q) are discussed in Section 3.2.

²⁵ Note that, following the usual convention (Gould 2004), the parallax parameters π_E are defined in the geocentric frame at the peak of the event as seen from Earth. Hence, (t_0 , u_0) are, almost by construction, nearly identical for the ground-only and joint solutions.

²⁶ For the finite-size source calculation, limb darkening may, in principle, be taken into account; however, the solution turns out to be in a region of the ρ , s , q parameter space, namely, with the source always passing far enough from the caustic, where it has no significant effect.

Table 2
2L1S Solutions with $\rho \neq 0$

Parameter	<i>Spitzer</i>	Ground	<i>Spitzer</i> and Ground	
χ^2/dof	39.4/34	2964.0/2935	3002.0/2974 (+, +)	3001.0/2974 (-, -)
t_0 [HJD-2,457,940.]	$-0.195^{+0.010}_{-0.010}$	$0.7677^{+0.0065}_{-0.0066}$	$0.7698^{+0.0059}_{-0.0058}$	$0.7701^{+0.0059}_{-0.0058}$
u_0	$0.1390^{+0.0085}_{-0.0082}$	$0.2395^{+0.0040}_{-0.0055}$	$0.2389^{+0.0034}_{-0.0040}$	$-0.2392^{+0.0038}_{-0.0032}$
t_E [days]	$14.38^{+0.65}_{-0.61}$	$14.68^{+0.17}_{-0.11}$	$14.70^{+0.14}_{-0.11}$	$14.69^{+0.13}_{-0.11}$
ρ	$0.0241^{+0.0058}_{-0.0078}$...	$0.0269^{+0.0026}_{-0.0034}$	$0.0270^{+0.0024}_{-0.0027}$
$\pi_{E,N}$	$-0.0782^{+0.0016}_{-0.0015}$	$0.0789^{+0.0014}_{-0.0015}$
$\pi_{E,E}$	$0.0531^{+0.0007}_{-0.0008}$	$0.0528^{+0.0007}_{-0.0007}$
α [rad]	$2.557^{+0.011}_{-0.012}$	$2.540^{+0.012}_{-0.011}$	$2.539^{+0.0076}_{-0.0074}$	$-2.5388^{+0.0067}_{-0.0069}$
s	$0.857^{+0.027}_{-0.028}$	$0.871^{+0.026}_{-0.022}$	$0.870^{+0.014}_{-0.014}$	$0.871^{+0.012}_{-0.013}$
q	$0.0080^{+0.0014}_{-0.0012}$	$0.0072^{+0.0012}_{-0.0011}$	$0.0073^{+0.0008}_{-0.0007}$	$0.0072^{+0.0007}_{-0.0006}$
$f_{s,\text{OGLE}}$...	1.138 ± 0.024	1.136 ± 0.019	1.138 ± 0.018
$f_{b,\text{OGLE}}$...	0.231 ± 0.024	0.232 ± 0.019	0.231 ± 0.018
$f_{s,\text{Spitzer}}$	17.9 ± 1.1	...	17.7 ± 0.3	17.7 ± 0.3
$f_{b,\text{Spitzer}}$	1.9 ± 1.0	...	2.0 ± 0.3	2.0 ± 0.3
$I - L$	2.982 ± 0.008	2.980 ± 0.007

light curve is sufficiently impacted to measure the planetary parameters.

The geometry shown in Figure 2 is of the so-called “(+, +)” solution, i.e., with $u_0 > 0$ for both ground-based and *Spitzer* observatories.²⁷ For 1L1S parallaxes, there is a generic fourfold degeneracy corresponding to the four possible sign combinations as seen from Earth and the satellite, i.e., (+, +), (+, -), (-, +), and (-, -). These can also be expressed as (+, -) \times (same, opposite), where the first component gives the sign of u_0 as seen from Earth and the second tells whether the satellite u_0 has the “same” or “opposite” sign. For well-covered binary lenses, we expect that the “(same, opposite)” degeneracy will be broken, although if good coverage is lacking, this degeneracy may persist (Zhu et al. 2015). Figure 2 illustrates this principle very well. We can see that if the Earth trajectory were transposed to the opposite side of the host (but with the same direction), it would be impacted by several cusps and caustics, so that its magnification profile would completely fail to match the observed light curve. Indeed, we confirm by numerical modeling that there are no viable “opposite” [(+, -) and (-, +)] solutions. However, there is a competitive (-, -) solution, the parameters of which are given in Table 2. As is often the case (Skowron et al. 2011), these parameters are nearly the same as for (+, +), except for the sign reversals of (u_0 , α , $\pi_{E,N}$).

Comparing Tables 1 and 2, we see that there is $\Delta\chi^2 = 22.9$ improvement for the (+, +) solution when adding ρ as a free parameter (and $\Delta\chi^2 = 24.9$ for (-, -)). The physical origin of this measurement lies in the narrowness of the magnification ridge that extends from the cusp seen in Figure 2, which is of the same order as the normalized source size. This is qualitatively similar to the case of OGLE-2016-BLG-1195Lb (Bond et al. 2017; Shvartzvald et al. 2017). Because ρ is not constrained at all in the ground-only models (see Table 2), one might suspect that the χ^2 improvement comes entirely from the *Spitzer* data. In fact, this is not the case: for the (+, +) solution,

only $\Delta\chi^2_{\text{Spitzer}} = 11$ comes from *Spitzer*, with the rest coming from the ground. Comparing Tables 1 and 2, we see that the (s , q) values for *Spitzer*-only and ground-only agree significantly better in the latter than the former. Moreover, the (s , q) values of the joint solution in Table 2 are nearly identical to those of the ground-only solution. This means that the ground-only model in Table 1 has been forced away from its “preferred” solution by the necessity to accommodate adjustments in (s , q) that are needed to reconcile the $\rho = 0$ model to the *Spitzer* data. Once ρ is set free in Table 2, the *Spitzer*-only model comes much closer to the (s , q) preferred by the ground-only model. In brief, the ground-based data act to “enforce” (s , q), and this indirectly places constraints on ρ . This leads to a factor of ~ 2 reduction in the error on ρ of the joint solution compared to the *Spitzer*-only solution, despite the fact that the ground-based data contain no direct information about ρ .

4. Physical Parameters

Because π_E and ρ are both measured, it is only necessary to determine θ_* in order to measure the physical properties of the system. We will then obtain $\theta_E = \theta_*/\rho$ and thereby the lens mass M and lens-source relative parallax π_{rel} ,

$$M = \frac{\theta_E}{\kappa\pi_E}, \quad \pi_{\text{rel}} = \theta_E\pi_E, \quad (4)$$

where $\kappa \equiv 4G/c^2\text{au} \simeq 8.144 \text{ mas } M_\odot^{-1}$ (see, e.g., Gould 2000 for an introduction to the concepts and formalism of microlensing).

4.1. Information from Microlens Parallax Only

Nevertheless, it is instructive to ask what can be known without the θ_E measurement, particularly because, for the overwhelming majority of the nonplanetary “comparison sample” needed to determine the Galactic distribution of planets, θ_E is not measured (Zhu et al. 2017).

²⁷ See Figure 4 from Gould (2004) for the definition of the sign of u_0 .

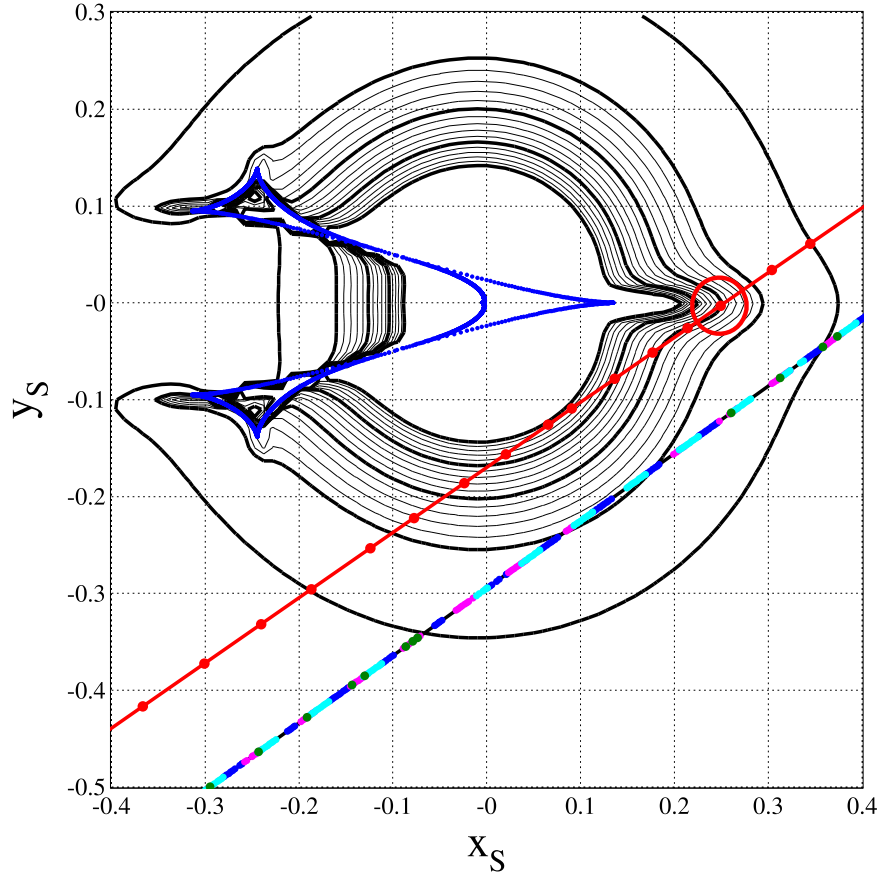


Figure 2. Lens geometry for the “(+, +)” 2L1S model of OGLE-2017-BLG-1140. The caustic structure is shown by a closed concave polygon. The point-source magnification contours for $A_{\text{point-source}} = (3, 4, 5, 6, 7)$ are shown by thick lines, with finer grading shown by thin lines. The two source trajectories (space and ground) are populated by source positions (relative to the lens structure) at the times of the observations. These are color-coded by observatory. The source size is shown as an open red circle. This illustrates how the source is resolved by the “magnification ridge” that extends from the cusp along the x -axis.

Table 3
Physical Parameters

Parameter	(+, +)	(-, -)
$M_{\text{host}} (M_{\odot})$	$0.213^{+0.036}_{-0.027}$	$0.211^{+0.032}_{-0.025}$
$M_{\text{planet}} (M_{\text{Jup}})$	$1.62^{+0.41}_{-0.29}$	$1.59^{+0.35}_{-0.26}$
$D_{8.3}$ (kpc)	$7.36^{+0.11}_{-0.14}$	$7.36^{+0.10}_{-0.12}$
θ_E (mas)	$0.164^{+0.028}_{-0.020}$	$0.163^{+0.024}_{-0.019}$
π_E	$0.0946^{+0.0014}_{-0.0016}$	$0.0949^{+0.0014}_{-0.0015}$
π_{rel} (mas)	$0.0155^{+0.0027}_{-0.0019}$	$0.0154^{+0.0023}_{-0.0019}$
μ_{rel} (mas yr $^{-1}$)	$4.07^{+0.69}_{-0.50}$	$4.04^{+0.60}_{-0.48}$
$\tilde{v}_{\text{hel,N}}$ (km s $^{-1}$)	$-1030.7^{+8.4}_{-8.7}$	$1030.9^{+8.3}_{-8.2}$
$\tilde{v}_{\text{hel,E}}$ (km s $^{-1}$)	728^{+13}_{-13}	719^{+13}_{-13}

We begin by calculating the heliocentric projected velocity for the two solutions in Table 2 (see also Table 3 below),

$$\tilde{\mathbf{v}}_{\text{hel}} = \tilde{\mathbf{v}}_{\text{geo}} + \mathbf{v}_{\oplus,\perp} \equiv \frac{\text{au}\pi_E}{\pi_E t_E} + \mathbf{v}_{\oplus,\perp}, \quad (5)$$

which, in equatorial coordinates, can be evaluated,

$$\tilde{\mathbf{v}}_{\text{hel}}(N, E) = \begin{bmatrix} (+1031, +719) \\ (-1031, +728) \end{bmatrix} \text{km s}^{-1} \begin{bmatrix} (-, -) \\ (+, +) \end{bmatrix}. \quad (6)$$

Here $\mathbf{v}_{\oplus,\perp} = (-0.8, +28.0) \text{km s}^{-1}$ is the velocity of Earth at the peak of the event, projected onto the plane of the sky. It is

notable that the direction of the $(-, -)$ solution (i.e., 35° north through east) is very similar to the direction of Galactic rotation. This would make it highly compatible with a disk lens. That is, in general,

$$\tilde{\mathbf{v}}_{\text{hel}} = \frac{\text{au}}{\pi_{\text{rel}}} \boldsymbol{\mu}_{\text{hel}}, \quad (7)$$

and so, ignoring the peculiar motions of the source, lens, and Sun, we expect that the projected velocity will lie almost exactly in the direction of Galactic rotation. This is because the local standard of rest (of the Sun) and the local standards of rest of other disk stars both partake of this motion, while the Galactic bar (the presumed home of the source) rotates in very nearly the same direction.

In fact, although this mean motion of the bar is usually ignored (but see Ryu et al. 2017), this is not strictly permissible in the present case because the Galactic longitude $l = 4.0$ is relatively high. Applying the law of sines and the exterior angle theorem, one finds that for solid-body rotation at Ω , the mean source proper motion is given by

$$\langle \boldsymbol{\mu}_s \rangle = \sin l (\cos l \cot \psi - \sin l) \Omega \rightarrow (\sin l \cot \psi) \Omega, \quad (8)$$

where ψ is the bar angle and we have eliminated second-order terms in the final expression. Adopting $\Omega = 75 \text{km s}^{-1} \text{kpc}^{-1}$ and $\psi = 40^\circ$, we obtain $\langle \mu_s \rangle = 1.3 \text{mas yr}^{-1}$ for this field.

Therefore, for disk lenses, we expect

$$\langle \mu_{\text{rel}} \rangle = \frac{v_{\text{rot}}}{D_S} - (\sin l \cot \psi) \Omega \rightarrow 4.3 \text{ mas yr}^{-1} \frac{v_{\text{rot}}}{v_{\text{rot}}}, \quad (9)$$

where v_{rot} is the velocity of Galactic rotation, $v_{\text{rot}} = |v_{\text{rot}}| \sim 220 \text{ km s}^{-1}$, and $D_S \sim 8.1 \text{ kpc}$ (see Section 4.3). Thus, while the direction of the lens-source relative motion of the $(-, -)$ solution (Equation (6)) favors disk lenses, the amplitude of the expected relative proper motion is actually very similar for both disk and bulge lenses.

Next, we insert this estimate of μ_{rel} for disk lenses and the value of \tilde{v} from Equation (6) to obtain

$$\langle \pi_{\text{rel}} \rangle = \frac{v_{\text{rot}}/D_S - (\sin l \cos \psi) \Omega}{\tilde{v}_{\text{hel}}} \text{ au} \rightarrow 0.016 \text{ mas}. \quad (10)$$

This means that the $(-, -)$ projected velocity is very nearly what would be expected for a disk lens with source-lens separation $D_{\text{LS}} \sim 1.0 \text{ kpc}$. In this case (and taking account of Equation (4)), we should have $\theta_E \simeq 0.17 \text{ mas}$, and so $M = \theta_E / \kappa \pi_E \simeq 0.22 M_{\odot}$. On the other hand, both solutions in Equation (6) are quite compatible with the lens being in the bulge, in which case π_{rel} would likely be slightly smaller, implying (at fixed π_E) smaller M and θ_E as well.

These arguments imply that, in the absence of any information about θ_E (the typical case for the nonplanetary ‘‘comparison sample’’), the microlens parallax measurement by itself would not discriminate well between bulge and disk lenses. This would not be particularly troubling for the comparison sample because it is used only to construct a comparison cumulative distribution of lens distances, so the role of any particular lens in this relatively large sample is quite minor (Calchi Novati et al. 2015a; Zhu et al. 2017).

However, it also shows that unless the measured lens-source relative proper motion turns out to be unexpectedly low (which would favor a bulge lens), this proper-motion measurement is unlikely, by itself, to add to the discriminatory power to what can be determined from the π_E measurement alone. We return to this point in Section 4.4.

4.2. Color–magnitude Diagram

Following Yoo et al. (2004), to measure $\theta_E = \theta_*/\rho$ we evaluate θ_* by placing the source on a color–magnitude diagram (CMD). However, because of high extinction, V_s is poorly measured, so we cannot place the source directly on an $[I, (V - I)]$ CMD. Instead, we use SMARTS (1.3 m) ANDICAM H -band data (together with OGLE I -band data) to derive $(I_{\text{OGLE-IV}} - H_{s,\text{ANDICAM}}) = -1.21 \pm 0.01$ in the instrumental system by aligning these to the best-fit model. We then calibrate this to the much deeper VVV catalog and find $H_{\text{ANDICAM}} - H_{\text{VVV}} = 4.65 \pm 0.01$ from field stars. This yields $(I_{\text{OGLE-IV}} - H_{s,\text{VVV}}) = 3.44 \pm 0.02$. From the fit to the light curve (Table 2), $I_{s,\text{OGLE-IV}} = 17.86 \pm 0.02$. We compare these values to those of the clump on the OGLE-IV/VVV CMD (Figure 3), $[(I - H), I]_{\text{cl}} = (3.50, 17.10) \pm (0.05, 0.08)$, and derive an offset $\Delta[(I - H), I] = (-0.06, +0.76) \pm (0.05, 0.08)$. Using the color–color relations of Bessell & Brett (1988), we translate this to an offset $\Delta[(V - I), I] = (-0.04, +0.76) \pm (0.05, 0.08)$ on the V/I CMD. We adopt $[(V - I), I]_{0,\text{cl}} = (1.06, 14.33)$ from Bensby et al. (2013) and Nataf et al. (2013) to finally

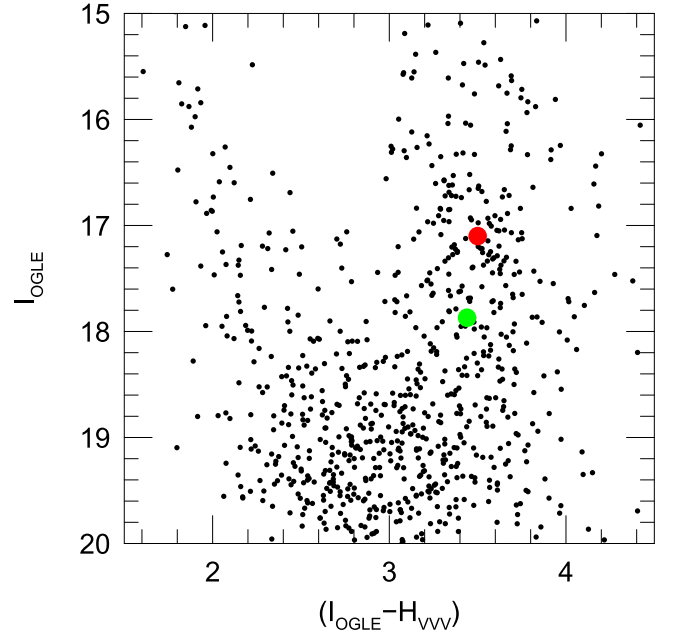


Figure 3. CMD from combining OGLE-IV I -band and VVV H -band data. The source position (green) in these two bands is determined from the best-fitting model to the OGLE I and SMARTS ANDICAM H , with the latter transformed to the VVV system from field stars. The clump centroid is shown in red.

derive $[(V - I), I]_{0,s} = (1.02, 15.09) \pm (0.05, 0.08)$. We then convert from V/I to V/K using the color–color relations of Bessell & Brett (1988), with $(V - K) = 2.36 \pm 0.12$. Finally, we use the Kervella et al. (2004) surface brightness relation to evaluate the angular diameter, θ_{LD} :

$$\log(\theta_{\text{LD}}) = 0.2672(V - K) + 0.5354 - 0.2 V. \quad (11)$$

The resulting source angular radius is

$$\theta_* = 4.39 \pm 0.38 \mu\text{as}. \quad (12)$$

We recall that, within this evaluation, based on the determination of the offset of the source within the CMD to the clump, the CMD itself does not need to be calibrated; specifically, zero-point offsets cancel out in the calculation. We also recall that the OGLE-IV I bandpass is extremely close to Cousins (Udalski et al. 2015a). In particular, the color term is well below the uncertainty of measurement of the clump centroid.²⁸

The final error budget for θ_* , relative error 8.7%, is dominated by the uncertainty in centroiding the clump and the conversion $(V - I, I)$ to $(V - K, K)$. Specifically, the error in the conversion of $(I - H)$ to $(V - I)$ is about 0.006 mag (this is because the offset from the clump is only 0.06 mag), well below the error in centroiding the clump, and so can be ignored. The relative error would drop to 3.2% if we neglected the error in centroiding the clump and to about 5.4% if we neglected the propagation error from $(V - I)$ to $(V - K)$. Finally, the error in the surface brightness relation is also negligible, with the relative error at the 1% level.

²⁸ Although this is not used in the evaluation, we note that $I_{\text{OGLE-IV}} = I_c + 0.094$.

4.3. Evaluation of Physical Parameters

Inserting the measurements of ρ and t_E from Table 2, the value in Equation (12) yields

$$\begin{aligned}\theta_E &= \frac{\theta_*}{\rho} = 0.16 \pm 0.02 \text{ mas}, \\ \mu_{\text{rel}} &= \frac{\theta_E}{t_E} = 4.1 \pm 0.6 \text{ mas yr}^{-1}.\end{aligned}\quad (13)$$

These values are very similar to those “predicted” in Section 4.1 for a disk lens prior to incorporating information about θ_E . As discussed there, this immediately implies that, although the lens distance is well measured, we cannot, on the basis of the microlensing solution alone, strongly discriminate between the lens lying in the disk or the bulge. We return to this problem in Section 4.4.

The simultaneous measurement of both the microlens parallax, π_E , and the Einstein angular radius, θ_E , together with that of the microlensing parameter $q = M_{\text{planet}}/M_{\text{host}}$, finally allow us to determine the physical parameters of the system (Equation (4)). In Table 3, we present the solution, and in particular we find

$$M_{\text{host}} = 0.21 \pm 0.03 M_{\odot}; \quad M_{\text{planet}} = 1.6_{-0.3}^{+0.4} M_{\text{Jup}}. \quad (14)$$

Note that in lieu of the lens distance, D_L , we rather report

$$D_{8.3} \equiv \frac{\text{kpc}}{1/8.3 + \pi_{\text{rel}}/\text{mas}}. \quad (15)$$

The primary reason for this is that $D_{8.3}$ is much better constrained than D_L because the error in the distance to the source (due to the finite depth of the bar) is of the same order as the distance from the lens to the source, $D_{\text{LS}} \equiv D_S - D_L$. Note that for cases like the present one, for which $D_{\text{LS}} \ll D_L$, we have approximately $D_{\text{LS}} \simeq 8.3 \text{ kpc} - D_{8.3}$. In particular, Calchi Novati et al. (2015a) introduced $D_{8.3}$ in order to put all *Spitzer* lenses on a homogeneous distance scale with minimal error.

However, we should also note that, at $l = 4.0$, the source is fairly far out on the near side of the Galactic bar and the value of $I_{\text{cl}} = 14.33$ adopted in Section 4.2 corresponds to a mean distance to the bar of $D_{\text{bar}} \sim 7.8 \text{ kpc}$. If the lens lay well in the foreground of the bar, then this would also be a good mean estimate for D_S . However, because the lens is either in or near the bar, the mean estimate of the source distance is “pushed back,” simply because the cross section for lensing scales $\sim \sqrt{D_{\text{LS}}}$. In particular, if the lens were known to be in the bar, the best estimate of the source distance would be $D_S = D_{\text{bar}} + D_{\text{LS}}/2 = 8.3 \text{ kpc}$. A similar effect (but not as strong) applies to disk lenses near the bar, $D_S \sim 8.0 \text{ kpc}$. We adopt $D_S \simeq 8.1 \text{ kpc}$ to evaluate the planet–host projected separation, a_{\perp} ,

$$a_{\perp} = 1.02 \pm 0.15 \text{ au}. \quad (16)$$

4.4. Source Proper Motion

We are fortunate that the source is a giant star that is relatively bright (despite significant extinction), relatively isolated, and only slightly blended. This means that we can measure the source proper motion μ_s , which will enable a much

more precise determination of the lens proper motion, $\mu_l = \mu_s + \mu_{\text{rel}}$, than would otherwise be possible. This can, in principle, provide a decisive kinematic discriminant between the bulge-lens and disk-lens interpretations. More specifically, as we will show, certain values of μ_l would decisively rule out disk lenses, but no measured value of μ_l would by itself decisively confirm the lens as belonging to the disk.

The rationale of the present analysis is to compare the estimated lens proper motion to that of the field bulge and MS (disk) populations. To estimate the relative probability of a disk versus a bulge lens, going beyond a possible “at-a-glance” analysis from Figure 4, we should take into account the underlying kinematic and density distributions for both populations. Below, we make a detailed evaluation of the relative probability based on the kinematic distributions. On the other hand, the disk and bulge density profiles at the lens distance toward this direction are too poorly understood at present to evaluate the density term of the relative probability. In the next few years, we may expect, following the GAIA DR2 release and therefore the knowledge of the astrometry of the bulge as a whole, to understand these density profiles much better. Together with the analysis presented here, this will then allow one to obtain a reliable estimate of the bulge-vs.-disk lens.

We begin by identifying three sets of stars from a CMD of stars in a $6'.5$ square centered on the event: 1008 bulge red clump (RC) stars, 2123 bulge red giant branch (RGB) stars, and 713 foreground MS stars. We measure the vector proper motions of each star (relative to a frame set by the RC stars) based on 250 (out of 708) better-seeing ($0''.9 < \text{FWHM} < 1''.3$) OGLE-IV images from $5275.9 \leq \text{HJD}' \leq 8019.6$. The typical proper-motion errors (derived from internal scatter) are $\sigma_{\mu} \sim 0.5 \text{ mas yr}^{-1}$. We exclude a handful of stars with individual errors $\sigma > 2 \text{ mas yr}^{-1}$. (The numbers given above already take account of this exclusion.) Figure 4 shows contours of the RC and MS proper-motion distributions based on smoothed counts and the proper motion of the source star:

$$\mu_s(N, E) = (0.86, -0.71) \pm (0.38, 0.36) \text{ mas yr}^{-1}. \quad (17)$$

Figure 4 also shows the lens proper motion μ_l together with an error ellipse (defined by covariance matrix c_{ij} , which we describe further below),

$$\begin{aligned}\mu_l(N, E) &= (4.21, 1.63) \text{ mas yr}^{-1}; \\ c_{ij} &= (1.10, 0.42, 0.42, 0.67), (\text{mas yr}^{-1})^2,\end{aligned}\quad (18)$$

where we have included the very small ($< 0.1 \text{ mas yr}^{-1}$) correction from geocentric to heliocentric proper motion.

From Figure 4, one sees that the lens proper motion is offset from the peak of the MS distribution by

$$\Delta\mu(N, E) = \mu_l - \mu_{\text{peak-MS}} = (0.56, -0.89) \text{ mas yr}^{-1}, \quad (19)$$

where $\mu_{\text{peak-MS}}(N, E) = (3.65, 2.52) \text{ mas yr}^{-1}$ is the peak of the MS distribution. To assess the level of consistency represented by this offset, we consider three sources of uncertainty. Two of these are error terms related to the measurement of $\mu_l = \mu_s + \hat{n}\mu_{\text{rel}}$, where $\hat{n} \equiv \mu_{\text{rel}}/\mu_{\text{rel}}$ is the direction of μ_{rel} , i.e., the same as the direction of $\tilde{\mathbf{v}}$. From Equation (17), the first-term covariance matrix is almost

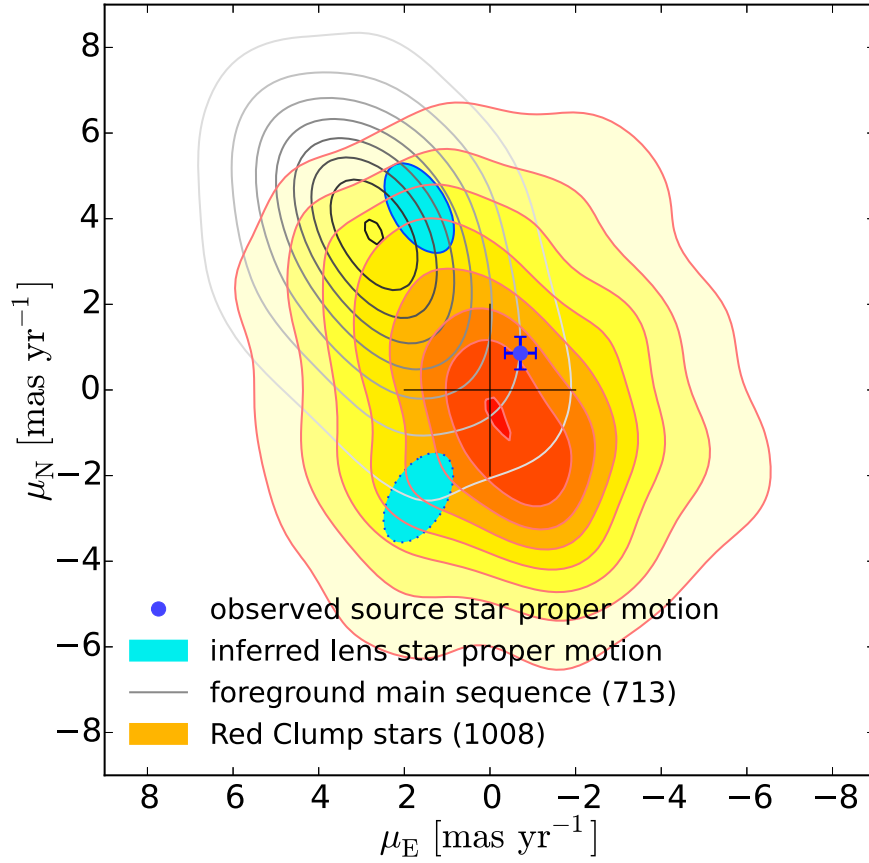


Figure 4. Smoothed proper-motion distributions of Galactic-bar RC stars and foreground disk MS stars. The source proper motion μ_s is well measured (blue point). Combining this with the two microlensing solutions in Table 2 yields two possible estimates for the lens proper motion μ_l (centers of cyan ellipses). The ellipses themselves take account of both the measurement errors entering into the determination of μ_l and the intrinsic proper-motion dispersion of disk lenses. See text for details. The northern and southern ellipses correspond to the $(-, -)$ and $(+, +)$ solutions, respectively.

isotropic. On the other hand, because \hat{n} is measured extremely well (see Table 2), the covariance matrix associated with μ_{rel} is nearly degenerate. Adding these two, we find $c_{ij}^{\text{meas}} = (0.35, 0.14, 0.14, 0.23)(\text{mas yr}^{-1})^2$.

The third source of uncertainty relates to the prediction of the lens proper motion under the assumption that the lens is in the disk. We assume that the velocity dispersion of the lenses is $(33, 18) \text{ km s}^{-1}$ in the rotational and vertical directions, i.e., similar to local disk stars. We then rotate to equatorial coordinates to obtain a covariance matrix $c_{ij}^{\text{pred}} = (0.75, 0.28, 0.28, 0.43)(\text{mas yr}^{-1})^2$. We can then evaluate the χ^2 of the measured offset $\Delta\mu$ given these uncertainties:

$$\chi_{\text{offset}}^2 = \sum_{ij} b_{ij}(\Delta\mu)_i(\Delta\mu)_j = 2.72; \quad b \equiv c^{-1};$$

$$c_{ij} = c_{ij}^{\text{meas}} + c_{ij}^{\text{pred}}. \quad (20)$$

For a 2D Gaussian, this has a probability $P(\chi_{\text{offset}}^2) = \exp(-\chi^2/2) = 0.26$, which is quite reasonable. From Figure 4, it is clear that the great majority of stars drawn randomly from the bulge population would have dramatically lower P values.

We note that, properly speaking, the c_{ij}^{meas} ellipse should be drawn around μ_l , while the c_{ij}^{pred} ellipse should be drawn around $\mu_{\text{peak-MS}}$. However, we have combined the two

covariance matrices (Equation (20)) for three reasons. First, from a mathematical standpoint, Equation (20) remains valid regardless of whether the contributing covariance matrices are summed before or after display. Second, with this display, the level of discrepancy is directly manifest in the diagram. Third, this mode of display will facilitate the numerical evaluations below.

We also show a second error ellipse²⁹ in the lower part of Figure 4. Any lens star that actually lay in this ellipse would (due to the $(+, +) \leftrightarrow (-, -)$ degeneracy; see Table 2) produce the same solutions as a corresponding star in the upper ellipse. Hence, the two groups of potential lenses can only be distinguished at the 1σ level and so must both be considered.

Assuming that the proper motions of lenses and sources are independent of their distances within the narrow limits permitted by the microlensing solution (a point to which we return below), the relative probability of a disk versus a bulge lens can be factored as

$$\frac{P_{\text{disk}}}{P_{\text{bulge}}} = \left(\frac{P_{\text{disk}}^{\text{kin}}}{P_{\text{bulge}}^{\text{kin}}} \right) \left(\frac{P_{\text{disk}}^{\text{dens}}}{P_{\text{bulge}}^{\text{dens}}} \right);$$

$$\frac{P_{\text{disk}}^{\text{kin}}}{P_{\text{bulge}}^{\text{kin}}} = \frac{f_{\text{disk}}^{(-,-)} + Qf_{\text{disk}}^{(+,+)}}{f_{\text{bulge}}^{(-,-)} + Qf_{\text{bulge}}^{(+,+)}}, \quad (21)$$

²⁹ $\mu_l(N, E) = (-2.51, 1.67) \text{ mas yr}^{-1}$; $c_l = (1.10, -0.42, -0.42, 0.66)(\text{mas yr}^{-1})^2$.

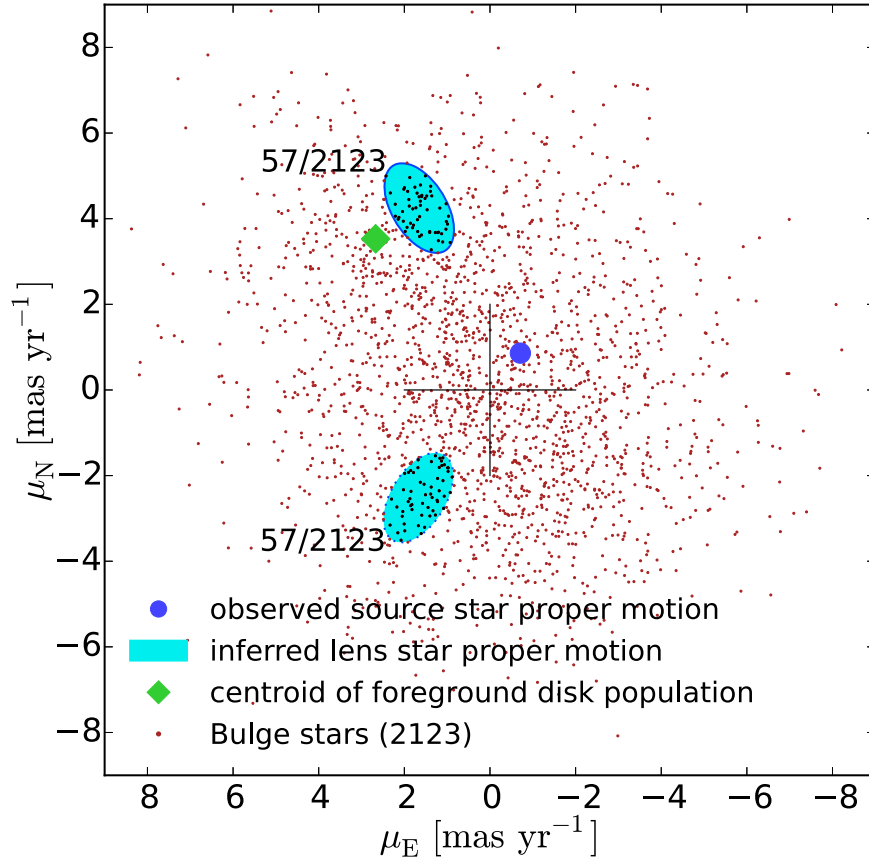


Figure 5. Observed proper motions of bulge RGB stars in a 6.5 square around OGLE-2017-BLG-1140. The cyan ellipses are the same as in Figure 4. The fractions of RGB stars that lie in each ellipse (57/2123 in both cases) enter the estimate of the relative kinematic probability of disk vs. bulge lenses. See Equation (23).

where $f_{\text{disk}}(\mu_l)$ and $f_{\text{bulge}}(\mu_l)$ are the normalized proper-motion distributions of the disk and bulge populations, respectively (convolved with measurement errors, as above), $f^{(-,-)}$ and $f^{(+,+)}$ are values of these distributions at the measured values of the two solutions, and $Q \equiv \exp(-(\chi_{\text{mod}(+,+)}^2 - \chi_{\text{mod}(-,-)}^2)/2) = 0.61$ is the relative likelihood of the microlensing models based on the χ^2 values in Table 2. We focus here on the first (kinematic) term, which is written more explicitly in the second expression of Equation (21).

As we describe below, the values of $f_{\text{bulge}}^{(-,-)}$ and $f_{\text{bulge}}^{(+,+)}$ can be evaluated purely empirically by counting RC (or RGB) stars in small areas in the neighborhoods of the two solutions and comparing these values to the total sample. However, the same principle cannot be applied to find $f_{\text{disk}}^{(-,-)}$ and $f_{\text{disk}}^{(+,+)}$ by counting MS stars. This is because the MS stars come from many different distances D along the line of sight. If, as in many Galactic models used to carry out Bayesian analyses (e.g., Han & Gould 1995), the rotation curve is assumed to be flat, then the mean proper motion of disk stars at any distance will always be the same. For this reason, it is appropriate to use the peak of the observed MS proper motions to evaluate the mean proper motion of disk stars at the distance of the lens, D_L . However, if (as also usually assumed) the velocity dispersions are independent of distance, then the proper-motion dispersions of disk stars scale $\sigma(\mu) \propto D^{-1}$. Since disk stars that are closer are systematically brighter at fixed luminosity (due both to proximity and lower extinction), the sample of MS stars is highly biased toward nearby stars with larger proper-motion

dispersions that are quite unrepresentative of stars at $D_L \sim 7$ kpc. It is for this reason that we evaluated c_{ij} , including both intrinsic dispersion and measurement errors. Therefore, we can write

$$P_{\text{disk}}^{\text{kin}} = f_{\text{disk}}^{(-,-)} + Q f_{\text{disk}}^{(+,+)} = \frac{\exp(-\chi_{\text{offset}}^2/2)}{2\pi\sqrt{|c|}} + Q \frac{\exp(-\chi_{\text{offset},(+,+)}^2/2)}{2\pi\sqrt{|c^{(+,+) }|}} \rightarrow \frac{\exp(-\chi_{\text{offset}}^2/2)}{2\pi\sqrt{|c|}} \quad (22)$$

where we have dropped the second term in the final expression because $\chi_{\text{offset},(+,+)}^2 = 55$. Noting that $\pi|c|^{1/2}$ is just the area of the error ellipse, we can now express the ratio of kinematic probabilities as

$$\frac{P_{\text{disk}}^{\text{kin}}}{P_{\text{bulge}}^{\text{kin}}} = \frac{\exp(-\chi_{\text{offset}}^2/2)/2}{(N_{\text{bulge}}^{(-,-)} + Q N_{\text{bulge}}^{(+,+)})/N_{\text{bulge}}} \rightarrow 3.0 \pm 0.3, \quad (23)$$

where we have made the evaluation using the RGB sample with $N_{\text{bulge}} = 2123$, and $N_{\text{bulge}}^{(-,-)} = 57$ and $N_{\text{bulge}}^{(+,+)} = 57$ are the numbers of RGB stars in the two ellipses shown in Figure 5.

Before continuing, we note that we performed a similar test but restricted it to the 1008 RC stars, which are basically a subset of the RGB sample but even less prone to contamination from foreground disk stars. We found 23 and 36 stars in the $(-, -)$ and $(+, +)$ ellipses. Inserting these numbers into Equation (23), we obtain $P_{\text{disk}}^{\text{kin}}/P_{\text{bulge}}^{\text{kin}} = 2.9 \pm 0.4$, which (even

Table 4
1L2S Solutions

Parameter	<i>Spitzer</i>	Ground	<i>Spitzer</i> and Ground	
χ^2/dof	94.2/35	2985.3/2936	3834.8/2975	3804.9/2975
			(+, +)	(+, -)
t_E [days]	$16.06^{+0.81}_{-0.74}$	$15.12^{+0.15}_{-0.15}$	$13.96^{+0.14}_{-0.17}$	$14.49^{+0.17}_{-0.17}$
$t_{0,1}$ [HJD—2,457,900.]	$37.022^{+0.023}_{-0.023}$	$36.337^{+0.040}_{-0.038}$	$37.698^{+0.031}_{-0.031}$	$38.163^{+0.057}_{-0.058}$
$t_{0,2}$ [HJD—2,457,900.]	$40.064^{+0.017}_{-0.016}$	$41.026^{+0.019}_{-0.019}$	$40.979^{+0.025}_{-0.025}$	$41.361^{+0.046}_{-0.047}$
$u_{0,1}$	$0.0299^{+0.0027}_{-0.0027}$	$0.0847^{+0.0050}_{-0.0048}$	$0.1808^{+0.0039}_{-0.0037}$	$0.2810^{+0.0088}_{-0.0081}$
$u_{0,2}$	$0.1237^{+0.0074}_{-0.0073}$	$0.2309^{+0.0041}_{-0.0041}$	$0.2752^{+0.0048}_{-0.0046}$	$0.2282^{+0.0057}_{-0.0054}$
$q_{f,I}$...	$29.5^{+3.3}_{-3.0}$	$15.6^{+1.7}_{-1.5}$	$2.75^{+0.23}_{-0.20}$
$q_{f,L}$	$19.7^{+2.1}_{-1.8}$...	$12.5^{+1.0}_{-1.0}$	$8.62^{+0.70}_{-0.61}$
$\pi_{E,N}$	$-0.1036^{+0.0021}_{-0.0023}$	$-0.2795^{+0.0058}_{-0.0061}$
$\pi_{E,E}$	$0.0500^{+0.0012}_{-0.0012}$	$0.0600^{+0.0021}_{-0.0021}$
$\Delta\tau_{\text{Ground}}$...	$0.3099^{+0.0038}_{-0.0038}$	$0.2355^{+0.0025}_{-0.0025}$	$0.2209^{+0.0034}_{-0.0034}$
$\Delta\tau_{\text{Spitzer}}$	$0.1894^{+0.0092}_{-0.0092}$...	$0.2342^{+0.0026}_{-0.0026}$	$0.2138^{+0.0031}_{-0.0031}$
$\Delta u_{0,\text{Ground}}$...	$0.1462^{+0.0072}_{-0.0072}$	$0.0944^{+0.0044}_{-0.0044}$	$-0.531^{+0.0043}_{-0.0043}$
$\Delta u_{0,\text{Spitzer}}$	$0.0939^{+0.0067}_{-0.0067}$...	$0.0892^{+0.0044}_{-0.0044}$	$0.0666^{+0.0045}_{-0.0045}$
$t_{0,1,\text{Spitzer}}$ [HJD—2,457,900.]	$36.865^{+0.030}_{-0.030}$	$37.075^{+0.028}_{-0.028}$
$t_{0,2,\text{Spitzer}}$ [HJD—2,457,900.]	$40.136^{+0.017}_{-0.017}$	$40.172^{+0.017}_{-0.017}$
$u_{0,1,\text{Spitzer}}$	$0.0523^{+0.0028}_{-0.0028}$	$0.0663^{+0.0032}_{-0.0032}$
$u_{0,2,\text{Spitzer}}$	$0.1415^{+0.0025}_{-0.0025}$	$0.1329^{+0.0025}_{-0.0025}$
$f_{s,\text{OGLE}}$...	1.069 ± 0.021	1.286 ± 0.026	1.172 ± 0.029
$f_{b,\text{OGLE}}$...	0.299 ± 0.021	0.082 ± 0.026	0.195 ± 0.029
$f_{s,\text{Spitzer}}$	15.3 ± 1.0	...	18.0 ± 0.3	17.0 ± 0.3
$f_{b,\text{Spitzer}}$	4.2 ± 0.7	...	2.3 ± 0.3	3.2 ± 0.3

considering that these are overlapping samples) is consistent at the 1σ level. Given that the sign of the difference is the opposite of what one would expect from greater contamination of the RGB sample, we adopt the RGB value (i.e., Equation (23)).

A more detailed analysis would require a more precise Galactic model than presently exists. Below, we outline some of the issues that would have to be addressed by such a model, but the key point is that vastly improved models are likely to be available within a year based on the *Gaia* DR2 data release. Hence, given the delicacy of the required calculations, it is premature to carry them out based on current Galactic models.

Here we just illustrate some of the issues that need to be considered. The first issue is that the assumption of constant velocity dispersion may well be incorrect. The scale heights of edge-on disks of external galaxies appear to be constant as a function of radius, while the radial density profiles are eponymously “exponential.” These simple observations argue for a vertical velocity dispersion that scales roughly as the square root of the surface density. However, by chance, any such adjustment would have a small effect in the present case. To see this, first note that (again by chance) $c_{ij}^{\text{pred}} \simeq 2c_{ij}^{\text{meas}}$. Therefore, if we were to, say, double the dispersions (i.e., multiply c_{ij}^{pred} by a factor of 4), this would increase c by a factor of 3.0. This would then change $P_{\text{disk}}^{\text{kin}}$ by a factor of $\exp(\chi_{\text{offset}}^2/3)/3 = 0.83$.

A second kinematic issue arises from possible streaming motions along the bar, which might, for example, be responsible for the elongated contours along the direction of the Galactic plane in the RC distribution shown in Figure 4.

The lens must be in front of the source (by $D_{\text{LS}} \sim 1$ kpc). Hence, if this streaming motion were primarily “outward” for stars in the closer side of the bar, then there would be a relatively big population of potential bulge lenses with proper motions strongly aligned with Galactic rotation. On the other hand, if the outward streaming motion were mainly on the more distant side of the bar (and the nearer side was streaming toward the Galactic center), then a bulge lens would be much less likely.

Finally, the density distribution of both the bar and the disk in this region must be estimated much more precisely than at present. For example, a very narrow bar would make it difficult to accommodate both a lens and a source, with $D_{\text{LS}} \sim 1$ kpc. Moreover, it is possible that the disk in the immediate neighborhood of the bar is depleted relative to an exponential profile due to action by the bar.

For these reasons, we defer a detailed calculation of $P_{\text{disk}}/P_{\text{bulge}}$ until more precise models are developed on the basis of the *Gaia* DR2 release.

5. A New Approach to Breaking the 2L1S/1L2S Degeneracy

The space-based and ground-based light curves are each reasonably well fit to 1L2S models. These models have six nonlinear parameters, $[(t_0, u_0)_{1,2}, t_E, q_f]$. Because there are two sources, there are two pairs of (t_0, u_0) , one for each source. The flux ratio q_f is assumed to be the same for all observations in the same band (in our case, *I* for ground-based data and *L* for *Spitzer* data). For fits with more than one band, there is one “ q_f ” for each band. Table 4 shows the fit parameters for *Spitzer*-only, ground-only, and joint 1L2S fits.

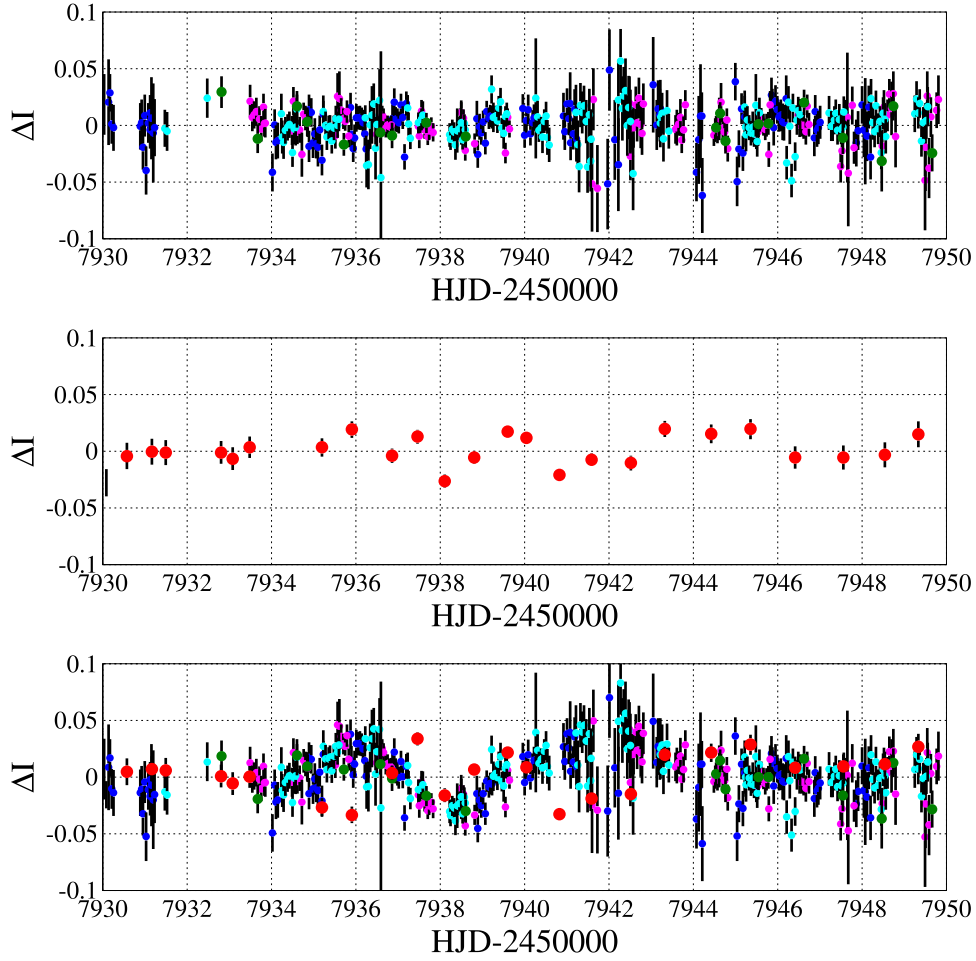


Figure 6. Residuals to 1L2S models for three cases: ground-only, *Spitzer*-only, and joint fits to all of the data. While the residuals shown in the top two panels are somewhat worse than those shown for the 2L1S case in Figure 1, the residuals for the joint fit (bottom panel) are dramatically worse. This is because the separate solutions are consistent with each other for 2L1S but not for 1L2S. See Section 5.

Comparing the χ^2 values to those in Table 2, we see that $\Delta\chi^2 \equiv \chi^2(1L2S) - \chi^2(2L1S)$ takes on values $\Delta\chi^2 = (+55, +19, +804)$ for the *Spitzer*-only, ground-only, and *Spitzer*+ground data sets, respectively. That is, whereas the 2L1S and 1L2S geometries yield models with qualitatively comparable χ^2 values when the ground-based data are analyzed alone and are moderately well distinguished based on *Spitzer* data alone, the 1L2S solution is decisively excluded for the joint fit to all data.

As a first step toward understanding the physical origin of this effect, we note that, whereas for 2L1S, $\chi_{\text{joint},2L1S}^2 = \chi_{\text{Spitzer},2L1S}^2 + \chi_{\text{ground},2L1S}^2 - 2$, for 1L2S, we find $\chi_{\text{joint},1L2S}^2 = \chi_{\text{Spitzer},1L2S}^2 + \chi_{\text{ground},1L2S}^2 + 725$. The approximate equality, $\chi_{\text{joint},2L1S}^2 \simeq \chi_{\text{Spitzer},2L1S}^2 + \chi_{\text{ground},2L1S}^2$, is expected from the fact (already noted in Section 3.1) that the *Spitzer*-only and ground-only 2L1S solutions are compatible with each other. This leads us to investigate whether the analogous 1L2S solutions are incompatible with each other.

To pursue this question further, we introduce for the 1L2S models the vector offset within the Einstein ring of the two sources,

$$(\Delta\tau, \Delta\beta)_{1L2S} \equiv \left(\frac{t_{0,2} - t_{0,1}}{t_E}, u_{0,2} - u_{0,1} \right). \quad (24)$$

Ignoring the very small motion of the binary source during the few days between the passage of the lens by the sources, these vector offsets should be the same as those seen by two different observers. However, we find from Table 4,

$$\begin{aligned} (\Delta\tau, \Delta\beta)_{\text{ground},1L2S} &= (+0.31, +0.15); \\ (\Delta\tau, \Delta\beta)_{\text{Spitzer},1L2S} &= (+0.19, +0.09). \end{aligned} \quad (25)$$

In particular, we note that the offsets in t_0 differ by about 1.7 days between models of the two data sets, whereas the errors in the individual measured values are all less than 0.04 day. Hence, in the joint solution, the two separately successful 1L2S models cannot be accommodated with a single $(\Delta\tau, \Delta\beta)_{1L2S}$. This inconsistency is illustrated by the residuals to the three fits, which are shown in Figure 6.

The fundamental origin for this incompatibility is that the magnification (actually, logarithm of magnification) falls off at different rates for binary-lens (or multi-lens) cusps than it does for point lenses. Of course, it is possible to arrange special geometries that avoid this problem. For example, if the impact parameter is the same as that seen by the two observatories, so that the same event essentially repeats at a later time, which can occasionally happen (Udalski et al. 2015b), then any 1L2S/2L1S degeneracy (or, indeed, any other degeneracy) will

persist. However, in the more generic case, we should expect that this degeneracy can be broken, provided that both observatories have some sensitivity to both bumps.

6. Discussion

OGLE-2017-BLG-1140 is the first anomalous microlensing event for which observation of the anomaly from both Earth and *Spitzer* was essential to the proper characterization of the anomaly. In particular, we showed that only by combining both data sets was it possible to decisively discriminate between the 2L1S and 1L2S interpretations. If this indeed represents a new path toward breaking this degeneracy, why is it appearing here for the first time?

For randomly selected microlensing events observed from two platforms, the relative strength of the anomalies observable at the two sites should be likewise randomly distributed. However, among the 18 published 2L1S events observed by *Spitzer*, OGLE-2017-BLG-1140 is only the second one for which the anomaly was stronger as observed by *Spitzer* than from the ground. In the other case, OGLE-2017-BLG-1130 (which, coincidentally, was alerted by OGLE and chosen as a “secret” *Spitzer* target at exactly the same time as OGLE-2017-BLG-1140), the anomaly was seen from *Spitzer* only³⁰ (Wang et al. 2018).

There are four factors that explain this apparent discrepancy. First, of the 18 2L1S events, five had short-timescale anomalies due to a planet.³¹ Because *Spitzer*’s cadence has typically been $\Gamma \sim 1 \text{ day}^{-1}$, it cannot in general be expected to characterize short-term anomalies in the absence of dense ground-based data over the anomaly. That said, it should be pointed out that OGLE-2017-BLG-1140 is one of these five events.

Second, the majority of *Spitzer* targets are near peak or have already peaked as seen from the ground at the time of the onset of *Spitzer* observations. This alone would imply that half or more of the anomalies that would be visible from *Spitzer*’s location are in fact missed by *Spitzer* observations. This late onset follows from the delay in *Spitzer* uploads (see Figure 1 of Udalski et al. 2015b) and the difficulty of recognizing and reliably choosing microlensing events based on their early evolution.

Third, due to the direction of Galactic rotation expressed in equatorial coordinates, more disk lenses are traveling east than west, meaning that they peak later as seen from *Spitzer*, which lies to the west of Earth. In itself, this is a relatively minor effect, but it exacerbates the previous one.

Fourth, *Spitzer* can observe targets that are near the ecliptic for a maximum of 38 days. Hence, for long events, anomalies can take place outside of the *Spitzer* window.

Taken together, these four effects mean that the new channel for resolving the 2L1S/1L2S degeneracy will not appear on a routine basis in *Spitzer* microlensing events. Nevertheless, it is worth noting that despite the relatively weak appearance of the OGLE-2017-BLG-1140 anomaly in ground-based data, the

³⁰ For two other events, the anomaly was of comparable strength as that seen from *Spitzer* and the ground: OGLE-2014-BLG-0124 (Udalski et al. 2015b) and OGLE-2015-BLG-1285 (Shvartzvald et al. 2015). Moreover, for two 1L1S events, finite-source effects were observed by *Spitzer* but not from the ground: OGLE-2015-BLG-0763 (Zhu et al. 2016) and OGLE-2015-BLG-1482 (Chung et al. 2017).

³¹ OGLE-2015-BLG-0966 (Street et al. 2016), OGLE-2016-BLG-1067 (Calchi Novati et al. 2018), OGLE-2016-BLG-1190 (Ryu et al. 2018), OGLE-2016-BLG-1195 (Bond et al. 2017; Shvartzvald et al. 2017), and OGLE-2017-BLG-1140 (this work).

addition of the also fairly modest signal from the *Spitzer* anomaly dramatically improved the confidence of the result. Further, although the anomaly was recognized in ground-based data soon after it occurred, the event was not systematically analyzed because it appeared to have insurmountable degeneracies. Therefore, it is quite possible that other archival events with even weaker, less noticeable anomalies can also yield interesting, unexpected results. Moreover, this same principle can be applied to future parallax-satellite missions, including *WFIRST* (Spergel et al. 2013), as well as other missions that are yet unplanned.

7. Conclusions

We have presented OGLE-2017-BLG-1140Lb, a microlensing extrasolar planet detected by combining ground-based survey, OGLE and KMTNet, and space-based, *Spitzer*, data. From the modeling point of view, this event is of particular interest. For the first time, *Spitzer*, besides providing the measure of the microlensing parallax, is essential for the characterization of the planetary system. Indeed, a deviation from the 1L1S Paczyński shape is apparent both from ground- (specifically, KMTNet) and space-based data, which are, however, separately each reasonably well fit by either a 1L2S or 2L1S planetary model. The analysis then leads us to show how the microlensing parallax opens a new path for breaking this classic degeneracy (Gaudi 1998) when combining ground- and space-based data. Specifically, we find that the 1L2S solution is ruled out by $\Delta\chi^2 \sim 800$ by the combined space/ground analysis, which is a factor of 10 higher than the $\Delta\chi^2 \sim 80$ from the sum of the ground and space analyses considered separately. As for the 2L1S planetary model, the system can be independently characterized by *Spitzer*, whose trajectory passes closer to the caustic structure, and ground-based data, leading to roughly the same configuration (except that ground-based data alone do not allow us to constrain the finite-source effect parameter, ρ). As we show, however, the combination of the two data sets puts a stronger constraint on the caustic structure (the binary parameter (s , q), i.e., the projected separation of the two lenses and their mass ratio, resulting specifically in a “resonant” configuration) and, indirectly, on ρ . The measurement of ρ , together with the photometric characterization of the source and the measurement of the microlens parallax, allow us to determine the physical parameters of the system. Specifically, we find $M_{\text{host}} = 0.21 \pm 0.03 M_{\odot}$ and $M_{\text{planet}} = 1.6_{-0.3}^{+0.4} M_{\text{Jup}}$, for a lens-to-source distance $D_{\text{LS}} \simeq 1 \text{ kpc}$ and a planet–host separation $a_{\perp} = 1.02 \pm 0.15 \text{ au}$, well beyond the system snow line. We show that the lens proper-motion analysis is consistent with the lens lying in the Galactic disk, although a bulge lens is not ruled out. In the framework of the *Spitzer* microlensing survey, OGLE-2017-BLG-1140Lb is the fifth planet to enter the sample for the determination of the Galactic distribution of exoplanets (Calchi Novati et al. 2015a; Zhu et al. 2017).

The discovery of OGLE-2017-BLG-1140Lb, a super-Jupiter-mass planet orbiting an M dwarf (beyond the system snow line), is also relevant in the larger framework of the microlensing statistical census of exoplanets (e.g., Gaudi 2012; Gould 2016). Indeed, out of 58 (microlensing) planets currently known,³² 11 belong to that same class (specifically, for a host mass $0.08 < M/M_{\odot} < 0.5$ and a planet mass larger than that

³² <https://exoplanetarchive.ipac.caltech.edu>

of Jupiter; e.g., Shvartzvald et al. 2014). OGLE-2017-BLG-1140Lb adds to this sample, and it is the fifth one belonging to the subsample of those with microlens parallax-based mass measurements, which are substantially more accurate. Notwithstanding the microlensing observational bias for the detection of such planetary systems (e.g., Batista et al. 2011), because of the abundance of M dwarfs and the detection efficiency's increase with q , the abundance of these systems, about 20% of all microlensing planets, remains a challenge for current planet-formation theories (e.g., D'Angelo et al. 2010).

The OGLE project has received funding from the National Science Centre, Poland, grant MAESTRO 2014/14/A/ST9/00121 to AU. Work by YKJ and AG was supported by AST-1516842 from the US NSF. IGS and AG were supported by JPL grant 1500811. This research has made use of the KMTNet system operated by the Korea Astronomy and Space Science Institute (KASI), and the data were obtained at three host sites of CTIO in Chile, SAAO in South Africa, and SSO in Australia. Work by YS was supported by an appointment to the NASA Postdoctoral Program at the Jet Propulsion Laboratory, California Institute of Technology, administered by Universities Space Research Association through a contract with NASA. Work by C. Han was supported by a grant (2017R1A4A1015178) of the National Research Foundation of Korea. This work is based (in part) on observations made with the *Spitzer Space Telescope*, which is operated by the Jet Propulsion Laboratory, California Institute of Technology, under a contract with NASA. Support for this work was provided by NASA through an award issued by JPL/Caltech. This work was partially supported by NASA contract NNG16PJ32C.

ORCID iDs

S. Calchi Novati  <https://orcid.org/0000-0002-7669-1069>
 J. Skowron  <https://orcid.org/0000-0002-2335-1730>
 B. S. Gaudi  <https://orcid.org/0000-0003-0395-9869>
 R. Poleski  <https://orcid.org/0000-0002-9245-6368>
 S. Kozłowski  <https://orcid.org/0000-0003-4084-880X>
 P. Pietrukowicz  <https://orcid.org/0000-0002-2339-5899>
 S.-J. Chung  <https://orcid.org/0000-0001-6285-4528>
 K.-H. Hwang  <https://orcid.org/0000-0002-9241-4117>
 Y.-H. Ryu  <https://orcid.org/0000-0001-9823-2907>
 I.-G. Shin  <https://orcid.org/0000-0002-4355-9838>

References

Afonso, C., Alard, C., Albert, J. N., et al. 2000, *ApJ*, 532, 340
 Alard, C., & Lupton, R. H. 1998, *ApJ*, 503, 325
 Albrow, M. D., An, J., Beaulieu, J.-P., et al. 2002, *ApJ*, 572, 1031
 Albrow, M. D., Horne, K., Bramich, D. M., et al. 2009, *MNRAS*, 397, 2099
 An, J. H. 2005, *MNRAS*, 356, 1409
 Batista, V., Gould, A., Dieters, S., et al. 2011, *A&A*, 529, A102
 Beaulieu, J.-P., Bennett, D. P., Fouqué, P., et al. 2006, *Natur*, 439, 437
 Bensby, T., Yee, J. C., Feltzing, S., et al. 2013, *A&A*, 549, A147
 Bessell, M. S., & Brett, J. M. 1988, *PASP*, 100, 1134

Bond, I. A., Bennett, D. P., Sumi, T., et al. 2017, *MNRAS*, 469, 2434
 Bozza, V. 2010, *MNRAS*, 408, 2188
 Calchi Novati, S., Gould, A., Udalski, A., et al. 2015a, *ApJ*, 804, 20
 Calchi Novati, S., Gould, A., Yee, J. C., et al. 2015b, *ApJ*, 814, 92
 Calchi Novati, S., Suzuki, D., Udalski, A., et al. 2018, submitted (arXiv:1801.05806)
 Chung, S.-J., Zhu, W., & Udalski, A. 2017, *ApJ*, 838, 154
 D'Angelo, G., Durisen, R. H., & Lissauer, J. J. 2010, in *Giant Planet Formation*, ed. S. Seager (Tucson, AZ: Univ. Arizona Press), 319
 Dominik, M. 1999, *A&A*, 349, 108
 Dong, S., Gould, A., Udalski, A., et al. 2009, *ApJ*, 695, 970
 Gaudi, B. S. 1998, *ApJ*, 506, 533
 Gaudi, B. S. 2012, *ARA&A*, 50, 411
 Gould, A. 1992a, *ApJL*, 386, 5
 Gould, A. 1992b, *ApJ*, 392, 442
 Gould, A. 1994, *ApJL*, 421, L75
 Gould, A. 1997, in *Variables Stars and the Astrophysical Returns of the Microlensing Surveys*, ed. R. Ferlet, J.-P. Maillard, & B. Raban (Gif-sur-Yvette, France: Editions Frontieres), 125
 Gould, A. 2000, *ApJ*, 542, 785
 Gould, A. 2004, *ApJL*, 606, 319
 Gould, A. 2016, in *Methods of Detecting Exoplanets, Astrophysics and Space Science Library*, Vol. 428, ed. V. Bozza, L. Mancini, & A. Sozzetti (Cham, Switzerland: Springer International), 135
 Gould, A., Carey, S., & Yee, J. 2013, *Spitzer Proposal ID*, 10036
 Gould, A., Carey, S., & Yee, J. 2014, *Spitzer Proposal ID*, 11006
 Gould, A., Yee, J., & Carey, S. 2015a, *Spitzer Proposal ID*, 12013
 Gould, A., Yee, J., & Carey, S. 2015b, *Spitzer Proposal ID*, 12015
 Gould, A., Yee, J., & Carey, S. 2016, *Spitzer Proposal ID*, 13005
 Griest, K., & Safizadeh, N. 1998, *ApJ*, 500, 37
 Han, C., & Gould, A. 1995, *ApJ*, 447, 53
 Han, C., Sumi, T., Udalski, A., et al. 2018, *AJ*, 155, 211
 Hwang, K.-H., Udalski, A., Bond, I. A., et al. 2017, in press (arXiv:1711.0965)
 Hwang, K.-H., Udalski, A., Shvartzvald, Y., et al. 2018, *AJ*, 155, 20
 James, F., & Roos, M. 1975, *CoPhC*, 10, 343
 Jung, Y. K., Udalski, A., Yee, J. C., et al. 2017, *AJ*, 153, 129
 Kervella, P., Bersier, D., Mourard, D., et al. 2004, *A&A*, 428, 587
 Kim, S.-L., Lee, C.-U., Park, B.-G., et al. 2016, *JKAS*, 49, 37
 Nataf, D. M., Gould, A., Fouqué, P., et al. 2013, *ApJ*, 769, 88
 Paczyński, B. 1986, *ApJ*, 304, 1
 Refsdal, S. 1966, *MNRAS*, 134, 315
 Ryu, Y.-H., Udalski, A., Bond, I. A., et al. 2018, *AJ*, 155, 40
 Ryu, Y.-H., Udalski, A., Yee, J. C., et al. 2017, *AJ*, 154, 247
 Shvartzvald, Y., Maoz, D., Kaspi, S., et al. 2014, *MNRAS*, 439, 604
 Shvartzvald, Y., Udalski, A., Gould, A., et al. 2015, *ApJ*, 814, 111
 Shvartzvald, Y., Yee, J. C., Calchi Novati, S., et al. 2017, *ApJL*, 840, L3
 Skowron, J., Ryu, Y.-H., Hwang, K.-H., et al. 2018, *AcA*, 68, 43
 Skowron, J., Udalski, A., Gould, A., et al. 2011, *ApJ*, 738, 87
 Spergel, D. N., Gehrels, N., Breckinridge, J., et al. 2013, arXiv:1305.5422
 Street, R., Udalski, A., Calchi Novati, S., et al. 2016, *ApJ*, 829, 93
 Tomaney, A. B., & Crotts, A. P. S. 1996, *AJ*, 112, 2872
 Udalski, A. 2003, *AcA*, 53, 291
 Udalski, A., Ryu, Y.-H., Sajadian, S., et al. 2018, *AcA*, 68, 1
 Udalski, A., Szymanski, M., Kaluzny, J., et al. 1994, *AcA*, 44, 227
 Udalski, A., Szymański, M. K., & Szymański, G. 2015a, *AcA*, 65, 1
 Udalski, A., Yee, J. C., Gould, A., et al. 2015b, *ApJ*, 799, 237
 Wang, T., Calchi Novati, S., Udalski, A., et al. 2018, submitted (arXiv:1802.09023)
 Woźniak, P. R. 2000, *AcA*, 50, 421
 Yee, J. C., Gould, A., & Beichman, C. 2015, *ApJ*, 810, 155
 Yee, J. C., Shvartzvald, Y., Gal-Yam, A., et al. 2012, *ApJ*, 755, 102
 Yoo, J., DePoy, D. L., Gal-Yam, A., et al. 2004, *ApJ*, 603, 139
 Zhu, W., Calchi Novati, S., Gould, A., et al. 2016, *ApJ*, 825, 60
 Zhu, W., Penny, M., Mao, S., Gould, A., & Gendron, R. 2014, *ApJ*, 788, 73
 Zhu, W., Udalski, A., Calchi Novati, S., et al. 2017, *AJ*, 154, 210
 Zhu, W., Udalski, A., Gould, A., et al. 2015, *ApJ*, 805, 8